# Two-Step Magnetic-Pulling Chemical Vapor Deposition Growth of CdS$_{1-x}$Se$_x$ Lateral Nanoribbon Heterostructures for High-Performance Photodetectors

*Xia Shen, Qihang Lv, Qian Yang, Jie Fan, Xiaohang Song, Pengfei Guo,* Pu Li, Johnny C. Ho,* and Kin Man Yu*

Bandgap integration in a single semiconductor nanostructure is an important task for their applications in photonics and photoelectronics. Herein a two-step growth of CdS$_x$Se$_{1-x}$ alloy nanoribbon heterostructures along the lateral direction by an improved two-step magnetic-pulling chemical vapor deposition (CVD) method is reported. Microstructural characterizations further demonstrate that these ribbons are formed by two separate components along the lateral direction of the nanoribbons, including CdS$_{0.76}$Se$_{0.24}$ at the central region and CdS$_{0.44}$Se$_{0.56}$ at both lateral sides, respectively. Under a laser excitation, photoluminescence spectrum and 2D emission mapping at the junctions show two different emission bands at 555 and 603 nm, which show agreement with the structural characterization results. More importantly, under 355 nm laser illumination, room-temperature dual-wavelength lasing with peak center at 542.3 and 605.2 nm is realized using these sandwich-like nanoribbons. Additionally, photodetectors based on these achieved nanoribbons are fulfilled with great performance of high responsivity ($2.4 \times 10^4$ A W$^{-1}$), high external quantum efficiency of $2.9 \times 10^5$%, fast response speed (rise $\approx$25 ms, decay $\approx$21 ms), and high $I_{on}/I_{off}$ ratio ($10^6$). These structures may offer an interesting system for exploring new applications in multifunctional nanophotonic and optoelectronic devices, such as high-performance detectors, miniature tunable lasers, and high-density color displays.

## 1. Introduction

Low-dimensional semiconductor heterostructures have attracted considerable attention as building blocks for applications in integrated photonic and optoelectronic devices and systems,[1–10] for example, nanoscale lasers,[6,11–13]

photodetectors,[14–18] light-emitting diodes,[19] optical switches,[20,21] field-effect transistors,[22] and solar cells[23] et al. In particular, group II–VI semiconductor heterostructure nanowires/ribbons, such as CdS/CdSSe,[14] ZnS/CdS/CdSe,[24] ZnO/ZnSe,[25] ZnS–ZnO,[26] ZnSSe–ZnSe,[15] bandgap-graded CdS$_{1-x}$Se$_x$,[27,28] and Zn$_y$Cd$_x$S$_{1-x}$Se$_{1-y}$,[29] are potential candidates for constructing multifunctional optoelectronic devices, owing to their controllable bandgaps, high quantum efficiency, and flexible synthesis methods.[22,30–34]

Since the discovery of carbon nanotubes, a large number of photodetectors and nanoscale lasers have been investigated based on 1D semiconductor heterostructures.[16,18,35,36] For instance, Wang et al. reported a ZnO/ZnS type-II heterojunction core/shell nanowire-based photodetector with enhanced performance through the piezophototronic effect.[16] Wan et al. reported ZnS$_{0.49}$Se$_{0.51}$/ZnSe axial heterostructure nanowire-based high-performance photodetectors by a two-step chemical vapor deposition (CVD) approach.[15] Shen et al. reported a (P3HT):CdSe nanowire heterojunction photodetector on silicon substrates, which exhibited greatly enhanced photocurrent.[18] However, it is still challenging to fabricate a wide spectral response and high-responsivity photodetector by a single lateral heterostructure ribbon due to the constraint of bandgap engineering, light absorptivity, and

**ADVANCED
SCIENCE NEWS**

www.advancedsciencenews.com

**ADVANCED
PHOTONICS
RESEARCH**

www.adpr-journal.com

photogenerated carriers transfer efficiency.[35,36] In addition, heterostructure nanowires or ribbons would serve as good waveguides and oscillating cavities as well as ideal gain materials.[11,37] Therefore, it is suggested that the heterostructures are ideal-model materials platforms for investigating multi-wavelength nanoscale lasers. So far, heterostructure nanowires, for example, CdS/CdSSe nanowires,[6] looped CdSSe alloyed nanowires,[38] and axially coupled wire cavities,[39] were successfully used to realize dual-color lasing or multicolor lasing.[40,41] Meanwhile, the growth of high-quality lateral heterostructures along a single nanoribbon is still very challenging due to the poor controllability of the solid evaporation sources under high temperature by the conventional synthesis method.[24,35,42]

In this work, we report the fabrication of $CdS_xSe_{1-x}$ lateral nanoribbon heterostructure by a two-step magnetic-pulling CVD approach. Structural investigation indicates the two semiconductor $CdS_xSe_{1-x}$ alloys ($CdS_{0.44}Se_{0.56}/CdS_{0.76}Se_{0.24}$) are epitaxially grown side by side at the lateral direction with sharp atomic interfaces. Microphotoluminescence (µ-PL) investigations at the heterojunction exhibit two different emission peaks at 555 and 603 nm, which is consistent with the structural analysis. Using these unique lateral structures, room-temperature dual-wavelength lasing at ≈542.3 and ≈605.2 nm is demonstrated under 355 nm pulse laser illumination. In addition, high-performance photodetectors are constructed, with high responsivity of $2.4 \times 10^4 A W^{-1}$, high external quantum efficiency (EQE) of $2.9 \times 10^5\%$, rapid response and recovery time (≈25 and 21 ms), and high $I_{on}/I_{off}$ ratio of $10^6$. These superior performances suggest the achieved heterojunction nanoribbons may have promising applications in integrated photonic and optoelectronic circuits.

## 2. Results and Discussion

The nanostructures are prepared by a two-step magnetic-pulling CVD method, as shown in Figure S1 (Supporting Information). A scanning electron microscopy (SEM) image in **Figure 1**A indicates that the as-grown nanoribbons have tens of micrometers in length, with width ranging from 0.5 to 6 µm and a thickness of ≈75 nm (Figure 1B). Figure 1C shows the real-color image of the nanoribbons on the original substrate under 405 nm laser illumination. Some typical ribbons (Figure 1D) were picked out and dispersed onto an $MgF_2$ substrate (refractive index: ≈1.39) for optical measurements. As shown, these selected nanoribbons have a peculiar structure with two different emission colors on both lateral sides and the central region. The well-defined interfaces suggest an abrupt change in the compositions between the lateral sides and the central region of the ribbons.

Transmission electron microscopy (TEM) combined with energy-dispersive X-Ray spectroscopy (EDX) was used to illustrate the microstructure and elemental composition of these nanoribbons. **Figure 2**A shows a typical TEM image of a representative nanoribbon with a uniform width of ≈4 µm. Figure 2B shows the EDX spectra collected from three different positions along the width direction of the ribbon (dots 1_3 in panel (A)), which reveal that positions 1 and 3 (lateral sides) mainly consist of Se and Cd elements with less S element (the detected Cu element originates from the microgrid), while position 2 (central region) is composed of abundant S and Cd elements and a small percentage of Se elements. It is demonstrated in Figure 2C–E 2D elemental mapping of a selected region of this ribbon (marked with a yellow rectangle in Figure 2A) for the detected elements, Cd, S, and Se, respectively. Obviously, the Cd element uniformly covers the entire region (Figure 2C), while S element is
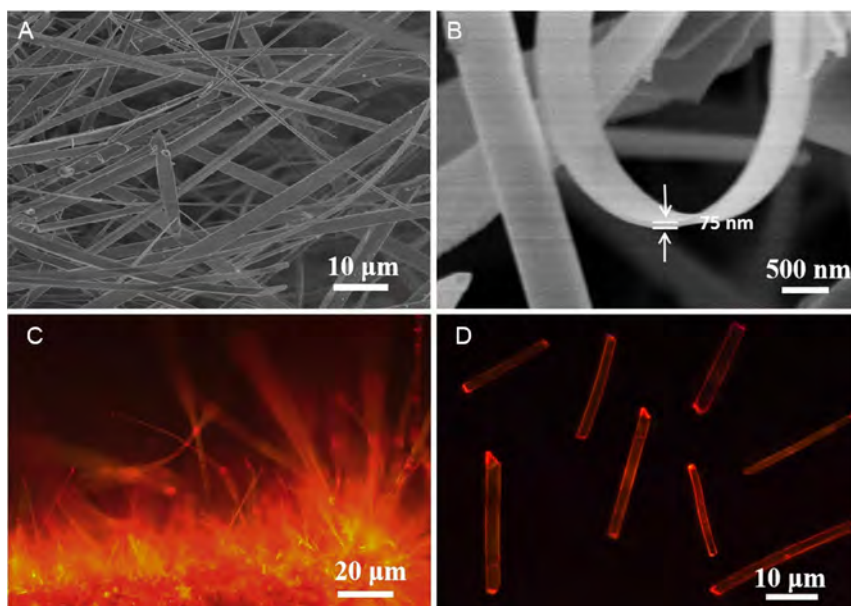


**Figure 1.** A) A Top-view low-resolution SEM image of the as-grown lateral heterostructure nanoribbons. B) A typical side-view SEM image of the heterostructure nanoribbon. The thickness of a ribbon is ≈75 nm. C) A dark-field real-color photograph of the heterostructure nanoribbons illuminated under an unfocused 405 nm laser. D) A typical real-color image of some selected heterostructure nanoribbons dispersed on an $MgF_2$ substrate.

**2200166 (2 of 7)**

ADVANCED
SCIENCE NEWS
www.advancedsciencenews.com

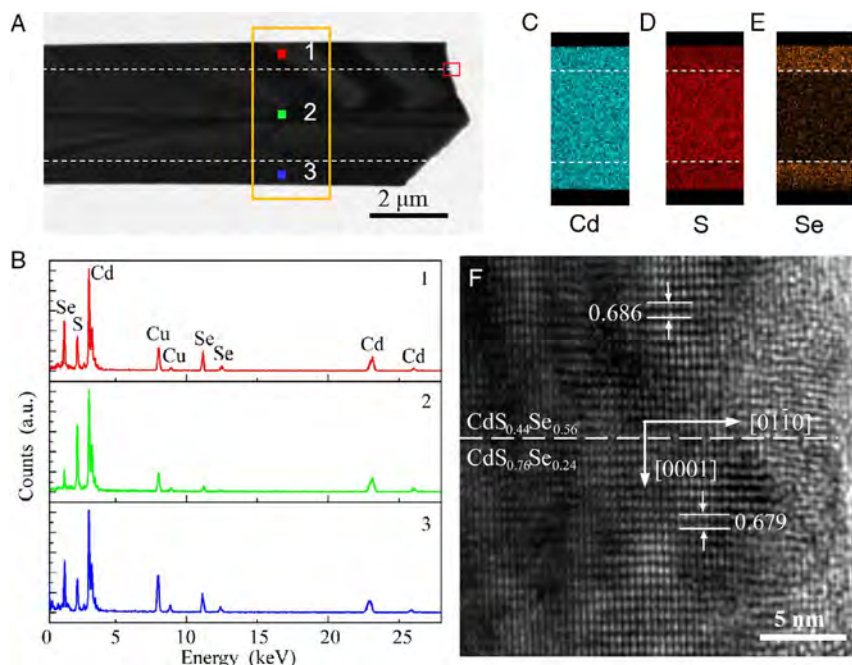ADVANCED
PHOTONICS
RESEARCH
www.adpr-journal.com

**Figure 2.** A) A low-resolution TEM image of a heterostructure nanoribbon and B) corresponding TEM–EDX profiles recorded from three typical positions (1-3) as indicated in panel A. C–E) 2D elemental mapping from the yellow box (in Figure A) of the ribbon for the three detected elements (Cd, S, and Se). F) HRTEM image recorded from the selected area (red square) of the heterostructure interface, as shown in (A).

distributed in the center (Figure 2D) and relatively less consistent in two lateral sides, and Se element is mostly distributed in two lateral sides (Figure 2E) inversely. Figure 2F shows a high-resolution TEM (HRTEM) image, taken from the tip of the interface region of the ribbon (see the red rectangle in Figure 2A), which exhibits a well-defined heterointerface between the central and lateral $CdS_xSe_{1-x}$ alloys, as indicated by a dashed line in Figure 2F. The measured lattice parameters in the center and lateral regions are 0.679 and 0.686 nm, which correspond to the distance of the (0001) plane of two composition wurtzite $CdS_xSe_{1-x}$ alloys with S mole fractions of $x \approx 0.44$ and 0.76, respectively. The structural analyses indicate that these ribbons are actually high-quality lateral heterostructures with an abrupt interface along the lateral direction of a single nanoribbon, which is commendably in agreement with real-color emission photographs. According to structural characterization, a proposed schematic diagram of the growth process of these heterostructure nanoribbons is shown in Figure S2 (Supporting Information), and the details of the growth process are discussed in the Experimental Section.

Spatially resolved PL spectra along the lateral direction of the nanoribbons were performed by a home-built confocal optical system (Figure S3, Supporting Information). **Figure 3**A shows the dark-field emission images ($a_1$–$a_5$) of a representative heterostructure nanoribbon along the lateral direction excited by a 488 nm laser. The corresponding PL spectra ($P_1$–$P_5$) are shown in Figure 3B. It can be seen that the PL spectra from both lateral sides ($P_1$, $P_5$) and the central region ($P_3$) of the ribbon show a strong single peak with wavelengths of 603 and 555 nm, respectively, which comes from the band-edge emissions of two different $CdS_xSe_{1-x}$ semiconductor alloys ($CdS_{0.44}Se_{0.56}$

and $CdS_{0.76}Se_{0.24}$). The PL spectra collected at the interface display two emission peaks, coming from both the central and lateral regions simultaneously. In addition, 2D PL mapping of a selected ribbon (Figure 3C) is exhibited in Figure 3D–G, in which two emission segments can be clearly observed. Figure 3E,G shows the wavelength-selected PL emission mapping extracted from Figure 3D in the spectral regions of 600–605 and 552–557 nm, respectively, corresponding to the PL spectra in Figure 3F,H, which exhibit that the dual-color emissions well spatially separated and distributed along the lateral direction of the ribbon. All these PL characterization results further indicate the laterally epitaxial growth of the heterostructures with two different semiconductor alloys.

Owing to the unique 1D geometry, the as-grown lateral heterostructure ribbons would serve as good oscillating cavities as well as ideal gain materials.[12,37,43] A dual-wavelength nanoscale laser was constructed using a single lateral heterostructure nanoribbon. **Figure 4**A shows a schematic diagram of the experimental setup for the measurement of the optically pumped nanowire lasers. The laser beam (Nd:YAG, 355 nm) is focused to $\approx 100\,\mu m$ by a microscope objective to provide optical pumping on these nanoribbons. The local optical signals are detected at the ribbon end by a CCD spectrometer. Figure 4B plots the pumping fluence-dependent PL spectra from an individual lateral heterostructure nanoribbon at room temperature. Two broad spontaneous emission bands with a peak centered at $\approx 555$ and $\approx 603$ nm are observed at a low pumping power fluence ($25\,kW\,cm^{-2}$), respectively. When the pump fluence increases to $56\,kW\,cm^{-2}$, a few sharp emission lines (at 599.9, 605.1, and 611.7 nm) start to appear, while the other broad emission band with a peak wavelength at $\approx 555$ nm shows no obvious

ADVANCED
SCIENCE NEWS
www.advancedsciencenews.com

ADVANCED
PHOTONICS
RESEARCH
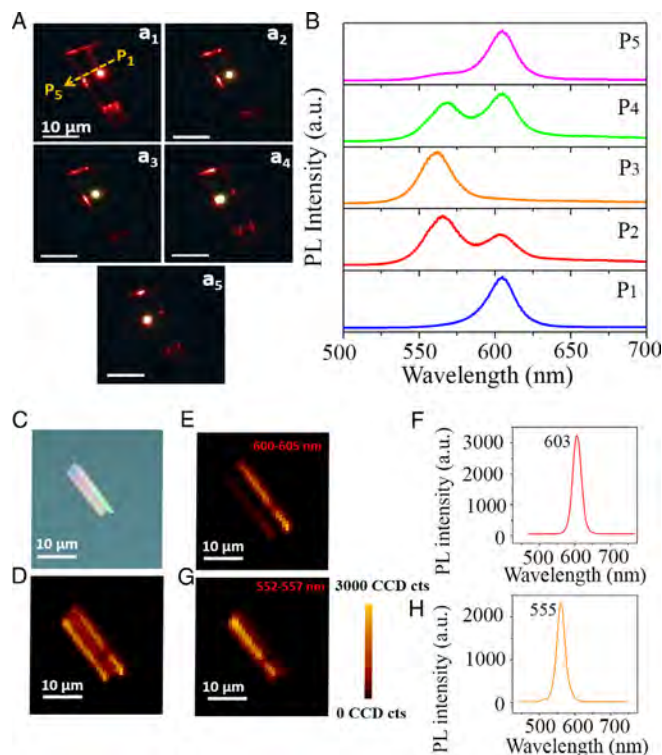Open Access

www.adpr-journal.com

**Figure 3.** A) Dark-field emission photographs ($a_1$–$a_5$) of a representative heterostructure nanoribbon excited by a 488 nm laser along the lateral direction. Scale bar is 10 µm. B) Corresponding normalized µ-PL spectra (position 1-5), as indicated in panel (A). C) An optical photograph of a typical heterostructure nanoribbon. D–G) 2D PL mapping images in the regions of 600–605 and 552–557 nm, which correspond to the µ-PL spectra in (F) and H), respectively.
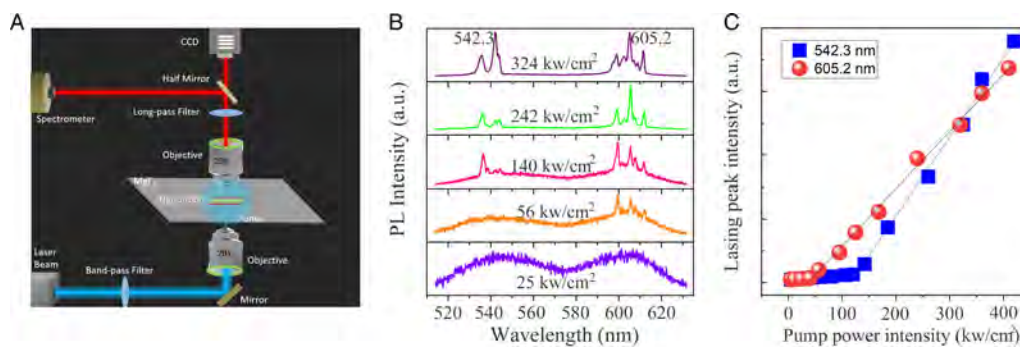


**Figure 4.** A) A schematic diagram of the experimental setup for the lasing measurements on a heterostructure nanoribbon. B) Pumping power-dependent room-temperature PL spectra from a heterostructure nanoribbon. C) Pumping power-dependent lasing intensity for the two emission peaks (542.3 and 605.2 nm), respectively.

changes at this stage. While further increasing the pump fluence up to 140 kW cm$^{-2}$, several sharp emission lines at 542.3 and 538.1 nm emerged around the broad emission band at 555 nm. The occurrence of these sharp emission lines from the two broad band-edge emission bands indicates the transition from spontaneous to stimulated emission.[44,45] When the pump fluence increases to 242 kW cm$^{-2}$ continuously, the intensity of the sharp emission line at 605.2 nm increases faster than other peaks clearly. Until the pump fluence rises above 324 kW cm$^{-2}$, the intensities of these two emission peaks at 542.3 and 605.2 nm are rapidly increased and proportionable at this point, and a

dual-wavelength lasing is successfully achieved (Figure S4, Supporting Information). The special bandgap structure of these heterostructure nanoribbons provides interesting active propagation and wavelength conversion simultaneously along the length of the ribbon, which is the key factor responsible for the observed dual-wavelength lasing. The orange light has larger absorption since the photon energy is larger than most of the bandgaps of $CdS_{0.44}Se_{0.56}$ alloy media. However, the photon energy of the lateral sides corresponds to a bandgap value smaller than the photon energy of the guided light. Thus, red lasing can receive additional optical gain from the wavelength of the orange

ADVANCED
SCIENCE NEWS
www.advancedsciencenews.com

ADVANCED
PHOTONICS
RESEARCH
www.adpr-journal.com

light during the active propagation of the guided light. The pumping fluence-dependent intensity of the lasing peaks at 542.3 nm (blue square) and 605.2 nm (red spheres) is shown in Figure 4C, respectively. It can be seen that the threshold of the lasing peak at 605.2 nm (56 kW cm$^{-2}$) is lower than the 542.3 nm peak (140 kW cm$^{-2}$), which can be further explained by the carrier transfer processes between the two emission bands of the heterostructures. When the excited light irradiates at the heterostructure nanoribbons, the photogenerated carriers from band-to-band transitions and the electron–hole pairs recombine radiatively, resulting in emitted photons. As the bandgap of $CdS_{0.44}Se_{0.56}$ is narrower than that of $CdS_{0.76}Se_{0.24}$, the emitted higher-energy photons from the wider bandgap could be reabsorbed by $CdS_{0.44}Se_{0.56}$ with the narrower bandgap followed by recombination and emission of lower-energy photons. Thus, the red emission at 605.2 nm (red spheres in Figure 4C) has a lower lasing threshold compared to the wide-bandgap emissions at 542.3 nm.

Photodetectors were constructed using these heterostructure nanoribbons, which are schematically shown in **Figure 5**A. Nanoribbons were first selected and transferred onto a Si/SiO$_2$ substrate. Then two Cr/Au (10 nm/80 nm) electrodes are constructed on the nanoribbons by a thermal deposited process. Figure 5B shows a typical SEM image of an as-fabricated device. Figure 5C exhibits the current−voltage ($I–V$) curves of the photodetector in the dark exposed under the illumination of a laser (4.18 mW cm$^{-2}$) with various wavelengths of 480,

532, 580, and 630 nm, respectively. It is worth to note the photocurrent increases observably when the device is illuminated by different wavelength lights, and the highest photoresponse of the device is observed at 532 nm. Figure 5D demonstrates the power density-dependent photoresponse of the nanoribbon photodetector under 532 nm light irradiation. As shown, the photocurrent exhibits a linear increase with the increase in pumping fluence. At a power density of 4.18 mW cm$^{-2}$, the photocurrent of the detector reaches $\approx 9.2 \times 10^{-5}$ A, which is about seven orders of magnitude higher than the dark current ($10^{-11}$ A). The responsivity as a function of wavelength is shown in Figure S5 (Supporting Information). These results revealed that the nanoribbon detector has high sensitivity. The inset in Figure 5D is a sublinear relationship for the pumping fluence-dependent photocurrent under 4 V bias. According to the definition of EQE for a photodetector[14,46]

$$EQE = hcR_\lambda/e\lambda \tag{1}$$

Here $R_\lambda = \Delta I/(PS)$ indicates the photodetector responsivity, $\Delta I$ is the difference between the photocurrent and dark current, $P$ is the incident light power density illuminated on the nanoribbons, $S$ is the area of the ribbon, and $\lambda$ is the wavelength of illuminated light. So the calculated responsivity $R_\lambda$ is $2.4 \times 10^4$ A W$^{-1}$, and the corresponding EQE is $2.9 \times 10^5$%. Figure 5E plots the photocurrent response of the photodetector illuminated by three different lights (480, 532, 580, and 630 nm) turned on and off
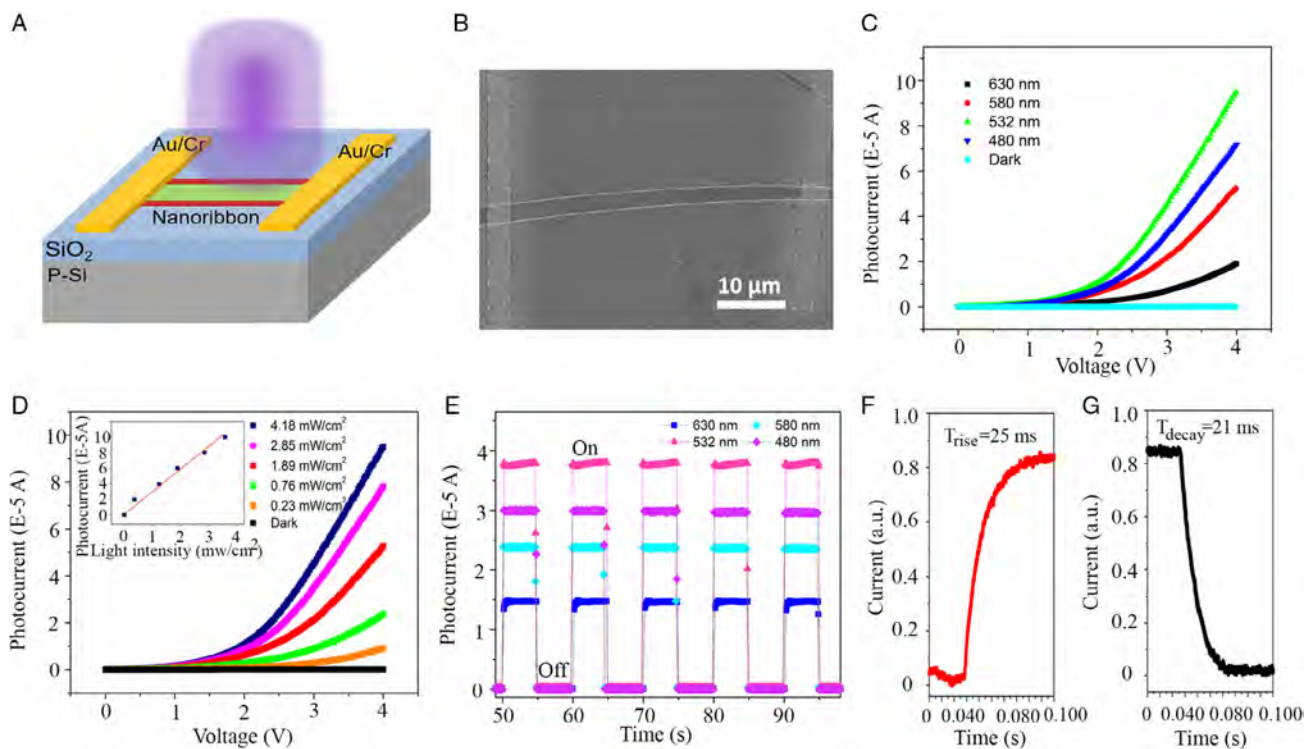


**Figure 5.** A) Schematic diagram of the heterostructure nanoribbon-based photodetector. B) SEM image of a fabricated device. C) $I–V$ curves of the device measured in the dark and under light illumination of different wavelengths (light intensity is 4.18 mW cm$^{-2}$). D) Photocurrent responsivity versus light intensity plot at a bias of 4 V. Inset shows the light density-dependent photocurrent at a voltage of 4 V. E) The reproducible $I_{on}/I_{off}$ switching upon 480, 532, 580, and 630 nm, respectively (light intensity is 2.9 mW cm$^{-2}$). F,G) Time-resolved photoresponse of the photodetector. The response time (the red curve) and recovery time (the black curve) of the photocurrent.

periodically at a bias voltage of 4 V. As shown, the photocurrent is generated rapidly while the detector is illuminated by a laser beam, and the photocurrent is largest when the irradiation light is 532 nm. The device also has a very high $I_{on}/I_{off}$ ratio of $10^6$, which is a reasonable range compared to the reported literature.[47–49] Figure 5F,G exhibits the rise time (25 ms) and decay time (21 ms) of the photodetector, which expressly reveals a rapid and effective response to the illuminated light, suggesting excellent properties of the photodetectors.

## 3. Conclusion

In conclusion, we report high-quality $CdS_xSe_{1-x}$ lateral heterostructure nanoribbons with abrupt interfaces by a two-step magnetic-pulling CVD method. High-performance photodetectors and dual-wavelength (542.3 and 605.2 nm) lasing are realized based on these heterostructure nanoribbons. The photodetector exhibits high performances with high responsivity ($2.4 \times 10^4 \, A \, W^{-1}$), high EQE ($2.9 \times 10^5\%$), fast response time (rise $\approx$25 ms, decay $\approx$21 ms), and high $I_{on}/I_{off}$ ratio ($10^6$). These lateral heterostructure-based photodetectors may have potential applications in the construction of integrated optoelectronic circuits and systems.

## 4. Experimental Section

*Material Preparation and Characterizations*: The nanoribbon lateral heterostructures were grown via a magnetic-pulling CVD method. Before the growth, an alumina boat with CdS powder (Alfa Aesar, 99.99%) was pulled into a quartz tube (inner diameter 45 mm, length 150 cm), which was located inside the heating zone of the horizontal furnace (OTF-1200X). The other boat with CdSe powder (Alfa Aesar, 99.99%) was placed upstream of the tube and located far enough away from the heating zone before growth. A quartz rod driven by a step motor through magnetic force was used to push the boats into/out of the heating zone. Several pieces of Si wafers (5 mm × 20 mm) coated with 2 nm-thick Au films were placed downstream of the gas flow to collect the products, as schematically shown in Figure S1, Supporting Information. Before heating, $N_2$ flow was introduced into the system at a rate of 200 sccm for 30–45 mins to purge the air inside the tube. The furnace temperature was then ramped to 850 °C at a rate of 50 °C min$^{-1}$, while maintaining the pressure at 300 mbar. After 45 min of growth, the temperature was reduced to 700 °C. Then, the other CdSe boat was then quickly pushed into the heating zone, and the growth was kept at 700 °C for an additional 20 min. After growth, the temperature was naturally reduced to room temperature.

*Optical Characterization*: The PL spectra were recorded by a homebuilt optical system. A 488 nm excitation laser beam was focused (spot size, $\approx$1 μm) by a microscope objective (Nikon, ×20) and then pumped locally on the nanoribbon heterostructures. The far-field optical images were recorded by a charge-coupled device color camera. The PL spectrum was recorded by Ocean Optics Spectrometer (Maya Pro2000). Stimulated emission properties were performed by a confocal optical system. A 355 nm pulse laser was focused to $\approx$100 μm and then pumped locally onto the nanoribbons. Optical photographs and PL spectrum were recorded by a noncolor CCD camera and Ocean Optics Spectrometer (LBS2500), respectively.

*Device Fabrication and Measurements*: The nanoribbon heterostructures were transferred to the highly doped p-type silicon substrates with a thermally grown 300 nm-thick $SiO_2$ layer. Then, the substrates were spin coated with MMA and PMMA, and electron beam lithography system (JEOL 6510 with NPGS) was employed to define the source and drain pattern. The Cr/Au (10 nm/80 nm) electrodes were completed by metal evaporation and lift-off processes. The current–voltage ($I-V$) characteristics of the nanoribbon photodetectors were measured using a Keithley 4200.

## Conflict of Interest

The authors declare no conflict of interest.

## Data Availability Statement

The data that support the findings of this study are available from the corresponding author upon reasonable request.

[1] M. Mogi, M. Kawamura, R. Yoshimi, A. Tsukazaki, Y. Kozuka, N. Shirakawa, K. S. Takahashi, M. Kawasaki, Y. Tokura, *Nat. Mater.* **2017**, *16*, 516.

[2] D. Yang, J. Liang, C. Zhou, L. Sun, R. Zheng, S. Luo, Y. Wu, J. Qi, *Adv. Opt. Mater.* **2016**, *4*, 1944.

[3] J.-M. Hu, L.-Q. Chen, C.-W. Nan, *Adv. Mater.* **2016**, *28*, 15.

[4] X. Hong, J. Kim, S.-F. Shi, Y. Zhang, C. Jin, Y. Sun, S. Tongay, J. Wu, Y. Zhang, F. Wang, *Nat. Nanotechnol.* **2014**, *9*, 682.

[5] X. Zhang, S. Yang, H. Zhou, J. Liang, H. Liu, H. Xia, X. Zhu, Y. Jiang, Q. Zhang, W. Hu, X. Zhuang, H. Liu, W. Hu, X. Wang, A. Pan, *Adv. Mater.* **2017**, *29*, 1604431.

[6] Q. Zhang, H. Liu, P. Guo, D. Li, P. Fan, W. Zheng, X. Zhu, Y. Jiang, H. Zhou, W. Hu, X. Zhuang, H. Liu, X. Duan, A. Pan, *Nano Energy* **2017**, *32*, 28.

[7] D. Li, M. Chen, Z. Sun, P. Yu, Z. Liu, P. M. Ajayan, Z. Zhang, *Nat. Nanotechnol.* **2017**, *12*, 901.

[8] H. Liu, D. Li, C. Ma, X. Zhang, X. Sun, C. Zhu, B. Zheng, Z. Zou, Z. Luo, X. Zhu, X. Wang, A. Pan, *Nano Energy* **2019**, *59*, 66.

[9] H. Liu, Y. Jiang, P. Fan, Y. Feng, J. Lan, G. Xu, X. Zhu, X. Zhang, X. Hu, T. Yang, B. Yang, Q. Zhang, D. Li, X. Wang, A. Pan, *Acs. Appl. Mater. Inter.* **2019**, *11*, 15813.

[10] P. Guo, W. Hu, Q. Zhang, X. Zhuang, X. Zhu, H. Zhou, Z. Shan, J. Xu, A. Pan, *Adv. Mater.* **2014**, *26*, 2844.

[11] Q. Zhang, R. Su, W. Du, X. Liu, L. Zhao, S. T. Ha, Q. Xiong, *Small Methods* **2017**, *1*, 1700163.

[12] C.-Z. Ning, L. Dou, P. Yang, *Nat. Rev. Mater.* **2017**, *2*, 17070.

[13] L. N. Quan, J. Kang, C.-Z. Ning, P. Yang, *Chem. Rev.* **2019**, *119*, 9153.

[14] P. Guo, J. Xu, K. Gong, X. Shen, Y. Lu, Y. Qiu, J. Xu, Z. Zou, C. Wang, H. Yan, Y. Luo, A. Pan, H. Zhang, J. C. Ho, K. M. Yu, *ACS Nano* **2016**, *10*, 8474.

[15] Z. Mu, Q. Zheng, R. Liu, M. W. I. Malik, D. Tang, W. Zhou, Q. Wan, *Adv. Electron. Mater.* **2019**, *5*, 1800770.

[16] S. C. Rai, K. Wang, Y. Ding, J. K. Marmon, M. Bhatt, Y. Zhang, W. Zhou, Z. L. Wang, *ACS Nano* **2015**, *9*, 6419.

[17] H. Lin, H. Liu, X. Qian, S.-W. Lai, Y. Li, N. Chen, C. Ouyang, C.-M. Che, Y. Li, *Inorg. Chem.* **2011**, *50*, 7749.

[18] X. Wang, W. Song, B. Liu, G. Chen, D. Chen, C. Zhou, G. Shen, *Adv. Funct. Mater.* **2013**, *23*, 1202.

[19] C. Pan, L. Dong, G. Zhu, S. Niu, R. Yu, Q. Yang, Y. Liu, Z. L. Wang, *Nat. Photonics* **2013**, *7*, 752.

[20] T. Zhai, L. Li, Y. Ma, M. Liao, X. Wang, X. Fang, J. Yao, Y. Bando, D. Golberg, *Chem. Soc. Rev.* **2011**, *40*, 2986.

[21] B. Piccione, C.-H. Cho, L. K. van Vugt, R. Agarwal, *Nat. Nanotechnol.* **2012**, *7*, 640.

[22] J. Xiang, W. Lu, Y. Hu, Y. Wu, H. Yan, C. M. Lieber, *Nature* **2006**, *441*, 489.

[23] L. Li, H. Lu, Z. Yang, L. Tong, Y. Bando, D. Golberg, *Adv. Mater.* **2013**, *25*, 1109.

[24] F. Fan, S. Turkdogan, Z. Liu, D. Shelhammer, C. Z. Ning, *Nat. Nanotechnol.* **2015**, *10*, 796.

[25] S. Yan, S. C. Rai, Z. Zheng, F. Alqarni, M. Bhatt, M. A. Retana, W. Zhou, *Adv. Electron. Mater.* **2016**, *2*, 1600242.

[26] W. Tian, C. Zhang, T. Zhai, S.-L. Li, X. Wang, J. Liu, X. Jie, D. Liu, M. Liao, Y. Koide, D. Golberg, Y. Bando, *Adv. Mater.* **2014**, *26*, 3088.

[27] X. Zhuang, P. Guo, Q. Zhang, H. Liu, D. Li, W. Hu, X. Zhu, H. Zhou, A. Pan, *Nano Res.* **2016**, *9*, 933.

[28] Z. Yang, D. Wang, C. Meng, Z. Wu, Y. Wang, Y. Ma, L. Dai, X. Liu, T. Hasan, X. Liu, Q. Yang, *Nano Lett.* **2014**, *14*, 3153.

[29] Z. Yang, J. Xu, P. Wang, X. Zhuang, A. Pan, L. Tong, *Nano Lett.* **2011**, *11*, 5085.

[30] J. Xu, L. Ma, P. Guo, X. Zhuang, X. Zhu, W. Hu, X. Duan, A. Pan, *J. Am. Chem. Soc.* **2012**, *134*, 12394.

[31] Z. Zheng, L. Gan, H. Li, Y. Ma, Y. Bando, D. Golberg, T. Zhai, *Adv. Funct. Mater.* **2015**, *25*, 5885.

[32] C. Zhang, Y. Yan, J. Yao, Y. S. Zhao, *Adv. Mater.* **2013**, *25*, 2854.

[33] P. Wan, M. M. Jiang, T. Xu, Y. Liu, X. S. Fang, C. X. Kan, *Adv. Opt. Mater.* **2022**, *10*, 2102315.

[34] J. X. Chen, W. Ouyang, W. Yang, J. H. He, X. S. Fang, *Adv. Funct. Mater.* **2020**, *30*, 1909909.

[35] L. Hu, J. Yan, M. Liao, H. Xiang, X. Gong, L. Zhang, X. Fang, *Adv. Mater.* **2012**, *24*, 2305.

[36] L. P. Hackett, M. A. Seyedi, M. Fiorentino, R. G. Beausoleil, *Appl. Phys.* **2017**, *50*, 215105.

[37] W. Eaton Samuel, M. Lai, A. Gibson Natalie, B. Wong Andrew, L. Dou, J. Ma, L.-W. Wang, R. Leone Stephen, P. Yang, *Proc. Natl. Acad. Sci. U.S.A.* **2016**, *113*, 1993.

[38] Y. Xiao, C. Meng, P. Wang, Y. Ye, H. Yu, S. Wang, F. Gu, L. Dai, L. M. Tong, *Nano Lett.* **2011**, *11*, 1122.

[39] C. Zhang, C.-L. Zou, H. Dong, Y. Yan, J. Yao, S. Zhao Yong, *Sci. Adv.* **2017**, *3*, e1700225.

[40] W. Zhang, J. Yao, Y. S. Zhao, *Acc. Chem. Res.* **2016**, *49*, 1691.

[41] S. W. Eaton, A. Fu, A. B. Wong, C.-Z. Ning, P. Yang, *Nat. Rev. Mater.* **2016**, *1*, 16028.

[42] J. Chen, W. Ouyang, W. Yang, J.-H. He, X. Fang, *Adv. Funct. Mater.* **2020**, *30*, 1909909.

[43] H. Zhu, Y. Fu, F. Meng, X. Wu, Z. Gong, Q. Ding, M. V. Gustafsson, M. T. Trinh, S. Jin, X. Y. Zhu, *Nat. Mater.* **2015**, *14*, 636.

[44] P. Guo, X. Zhuang, J. Xu, Q. Zhang, W. Hu, X. Zhu, X. Wang, Q. Wan, P. He, H. Zhou, A. Pan, *Nano Lett.* **2013**, *13*, 1251.

[45] P. Guo, M. K. Hossain, X. Shen, H. Sun, W. Yang, C. Liu, C. Y. Ho, C. K. Kwok, S.-W. Tsang, Y. Luo, J. C. Ho, K. M. Yu, *Adv. Opt. Mater.* **2018**, *6*, 1700993.

[46] L. Li, P. Wu, X. Fang, T. Zhai, L. Dai, M. Liao, Y. Koide, H. Wang, Y. Bando, D. Golberg, *Adv. Mater.* **2010**, *22*, 3161.

[47] T. Gao, Q. H. Li, T. H. Wang, *Appl. Phys. Lett.* **2005**, *86*, 173105.

[48] T. Takahashi, P. Nichols, K. Takei, A. C. Ford, A. Jamshidi, M. C. Wu, C. Z. Ning, A. Javey, *Nat. Nanotechnol.* **2012**, *23*, 045201.

[49] T. Zhai, X. Fang, M. Liao, X. Xu, L. Li, B. Liu, Y. Koide, Y. Ma, J. Yao, Y. Bando, D. Golberg, *ACS Nano* **2010**, *4*, 1596.